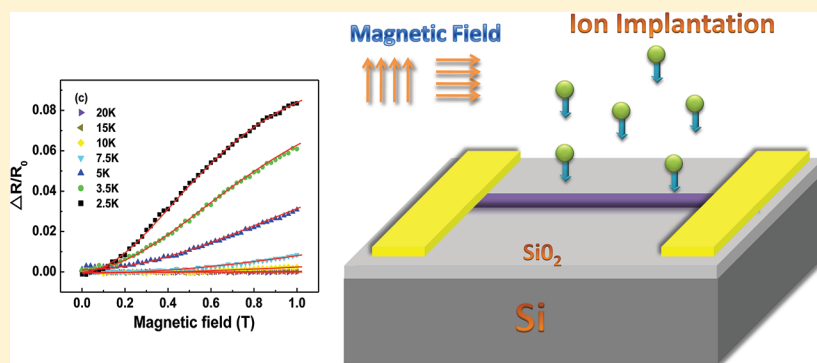


Tuning Quantum Corrections and Magnetoresistance in ZnO Nanowires by Ion Implantation

Y. J. Zeng,^{*,†} L. M. C. Pereira,[‡] M. Menghini,[†] K. Temst,[‡] A. Vantomme,[‡] J.-P. Locquet,[†] and C. Van Haesendonck[†]

[†]Laboratory of Solid-State Physics and Magnetism, Katholieke Universiteit Leuven, Celestijnenlaan 200 D, BE-3001 Leuven, Belgium

[‡]Instituut voor Kern-en Stralingsfysica, Katholieke Universiteit Leuven, Celestijnenlaan 200 D, BE-3001 Leuven, Belgium



ABSTRACT: Using ion implantation, the electrical as well as the magnetotransport properties of individual ZnO nanowires (NWs) can be tuned. The virgin NWs are configured as field-effect transistors which are in the enhancement mode. Al-implanted NWs reveal a three-dimensional metallic-like behavior, for which the magnetoresistance is well described by a semiempirical model that takes into account the presence of doping induced local magnetic moments and of two conduction bands. On the other hand, one-dimensional electron transport is observed in Co-implanted NWs. At low magnetic fields, the anisotropic magnetoresistance can be described in the framework of weak electron localization in the presence of strong spin–orbit scattering. From the weak localization, a large phase coherence length is inferred that reaches up to 800 nm at 2.5 K. The temperature-dependent dephasing is shown to result from a one-dimensional Nyquist noise-related mechanism. At the lowest temperatures, the phase coherence length becomes limited by magnetic scattering.

KEYWORDS: Nanowires, one dimensional, magnetotransport, ZnO, weak localization, ion implantation

Nanowires (NWs) with a large aspect ratio and a diameter below 100 nm have inspired worldwide research efforts due to the numerous unique properties that are expected for these (quasi-) one-dimensional (1D) systems, including electrical, optoelectronic, electromechanical, and photovoltaic properties.^{1–5} Among various materials, zinc oxide (ZnO), by virtue of its excellent material properties, such as a wide direct bandgap of 3.37 eV at room temperature and a large exciton binding energy of 60 meV as well as high electron mobility and high thermal conductivity, has attracted particular attention as a revival semiconductor.^{6–8} ZnO NWs have been used as main components in piezoelectric nanogenerators,⁹ field-effect transistors (FETs),¹⁰ blue/ultraviolet (UV) light emitters,¹¹ and solar cells.¹² On the other hand, transition-metal-doped ZnO has been considered as a promising dilute magnetic semiconductor due to the theoretically predicted high Curie temperature above room temperature.¹³ As a consequence, the ZnO-based dilute magnetic semiconductors may have great potential in the field of spintronics, where the central theme is the manipulation of both spin and charge degrees of freedom in solid-state systems.^{14,15} However, the magnetotransport prop-

erties of transition-metal-doped ZnO, which are essential for spintronics applications, still lack a proper understanding. Most magnetotransport studies have focused on thin film or bulk samples,^{16–20} while ZnO NWs were far less covered.²¹ This is not only due to the intrinsic difficulties for characterizing these wires but also because the controlled in situ doping with electronically and magnetically active impurities remains an important challenge for the NWs.²²

In this Letter, we demonstrate how the electrical as well as the magnetotransport properties of ZnO NWs can be tuned by ion implantation. With respect to applications, ion implantation offers a convenient way to control the dopant species and concentration as well as the doping position, which might overcome the difficulties of in situ doping in NWs. To better understand the effects of magnetic doping, magnetic cobalt (Co) as well as nonmagnetic aluminum (Al) are implanted into individual ZnO NWs. In particular, we observe 1D quantum

Received: October 4, 2011

Revised: December 5, 2011

Published: January 3, 2012

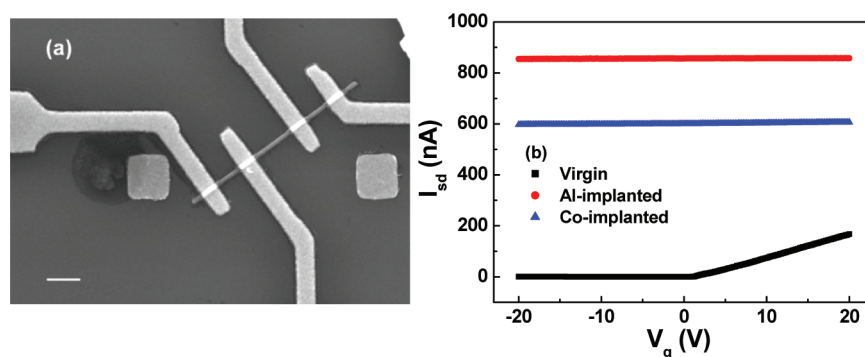


Figure 1. (a) SEM image of a Co-implanted ZnO NW FET device. The white scale bar corresponds to 1 μm . (b) Source–drain current as a function of gate voltage of a virgin, an Al-implanted, and a Co-implanted ZnO NW in the dark at room temperature. The source–drain bias voltage is 100 mV for the virgin NW and 20 mV for the implanted NWs.

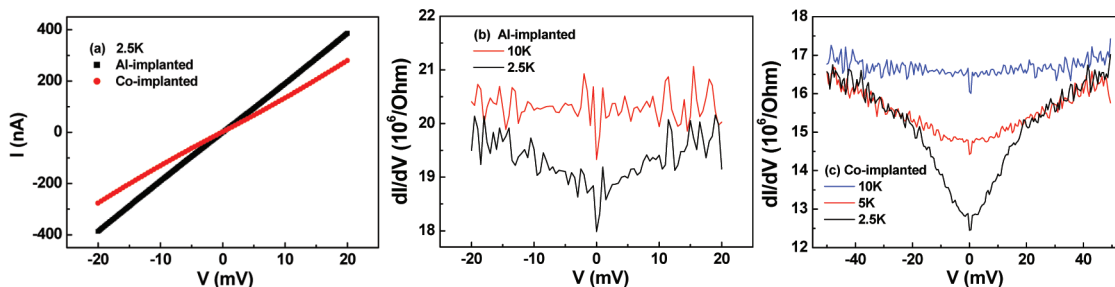


Figure 2. (a) I - V characteristics of implanted ZnO NWs at 2.5 K, and $dI/dV(V)$ curves of Al- (b) and Co-implanted (c) ZnO NWs at different temperatures.

corrections in Co-implanted ZnO NWs. The strong anisotropic magnetoresistance (MR), which is positive due to strong spin–orbit scattering, points to a large phase coherence length which reaches up to 800 nm at low temperature. A large phase coherence is of direct relevance for spintronics applications.

ZnO NWs were grown by catalyst-free vapor phase deposition and then dispersed in ethanol and transferred to heavily doped p-type silicon wafers with a top layer of 300 nm thick thermal oxide.²³ Al and Co ions were implanted into individual NWs lying on the Si/SiO₂ substrates at room temperature using an energy of 70 and 80 keV, respectively. Based on stopping range of ions in matter (SRIM) simulation,²⁴ ion implantation range and ion straggle were calculated to be 68 and 32 nm for Al and 37 and 16 nm for Co, respectively. Implantation fluences of 5×10^{15} , 7×10^{15} , 1×10^{16} , and 1.5×10^{16} ions/cm² were used. A fluence of 1×10^{16} ions/cm² corresponds to a peak concentration of 2.8% and 5.6% for Al and Co, respectively. In the following, we will present the typical results for a fluence of 1×10^{16} ions/cm², unless otherwise stated. After implantation, rapid thermal annealing at 400 °C was performed in nitrogen gas for 1 min to recover the crystalline structure of the ZnO NWs. In a next step, the ZnO NWs were imaged by scanning electron microscopy (SEM, JEOL JSM-5600), and electrical contacts were attached to individual NWs by electron beam lithography and lift-off techniques. A few seconds of in situ Ar ion milling was used to clean the NW surface before deposition of 10 nm of Ti followed by 150 nm of Au. The electrical properties of the ZnO NWs were measured in a FET configuration (Keithley, Model 4200-SCS), using the heavily doped Si substrates as the back gate electrode. MR measurements were performed in a helium-4 flow cryostat with a superconducting magnet (Oxford Instruments) using a low-frequency ac resistance bridge (Linear

Research, LR-700). The magnetic field H was carefully oriented either parallel or perpendicular to the axis of the NWs. The MR is defined as $[R(H) - R(H = 0)]/R(H = 0) \times 100\%$.

In Figure 1a we present an SEM image of a Co-implanted ZnO NW device with four attached Ti/Au electrical contacts. The typical diameter of the NWs selected for attaching electrical contacts is of the order of 100 nm to ensure the implanted ions are well inside the NWs. The difference between two- and four-probe resistance turns out to be less than 1% even at helium temperature, which implies the formation of good ohmic contacts due to the in situ ion milling. In Figure 1b we plot the FET transfer characteristics of a virgin, an Al-implanted, and a Co-implanted ZnO NW in the dark at room temperature. Our virgin NW FETs are in the enhancement mode (normally “off”), which implies the channel is totally depleted at zero gate voltage. The virgin ZnO NWs are therefore a good starting material to investigate the doping effects. On the other hand, the Al- and Co-implanted NWs (ion fluence of 1×10^{16} ions/cm²) carry a much higher current even at a smaller source–drain voltage of 20 mV, and they show negligible gate effect. This metallic-like behavior is also observed for two other implantation fluences, i.e., 7×10^{15} and 1.5×10^{16} ions/cm² (data not shown). We therefore conclude that the increased conductivity of the NWs results from the implanted dopants. In addition to negligible gate effect, the resistance of the Al- and Co-implanted NWs also has a weak temperature dependence: The resistance only increases by a factor of 1–2 at liquid helium temperature when compared to the resistance at room temperature. On the other hand, the resistance of the virgin NWs exponentially increases with decreasing temperature, indicative of the thermally activated behavior of a semiconductor. In the following, we will focus only on the behavior of the implanted NWs at low temperature.

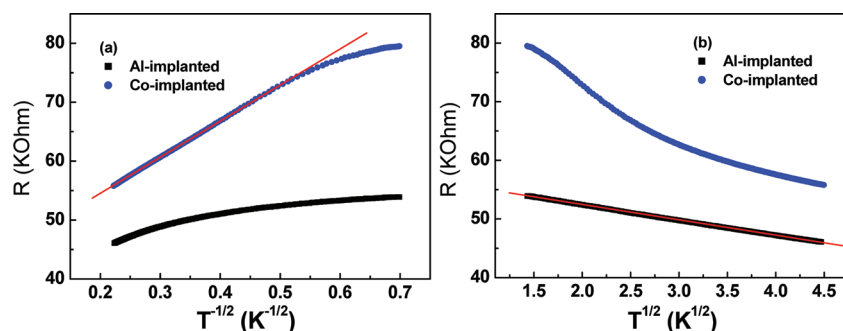


Figure 3. Temperature dependence of the resistance of implanted ZnO NWs: (a) 1D e–e interaction related corrections give rise to a $T^{-1/2}$ dependence, while (b) 3D e–e interaction related corrections result in a $T^{1/2}$ dependence. The red lines are guides to the eye.

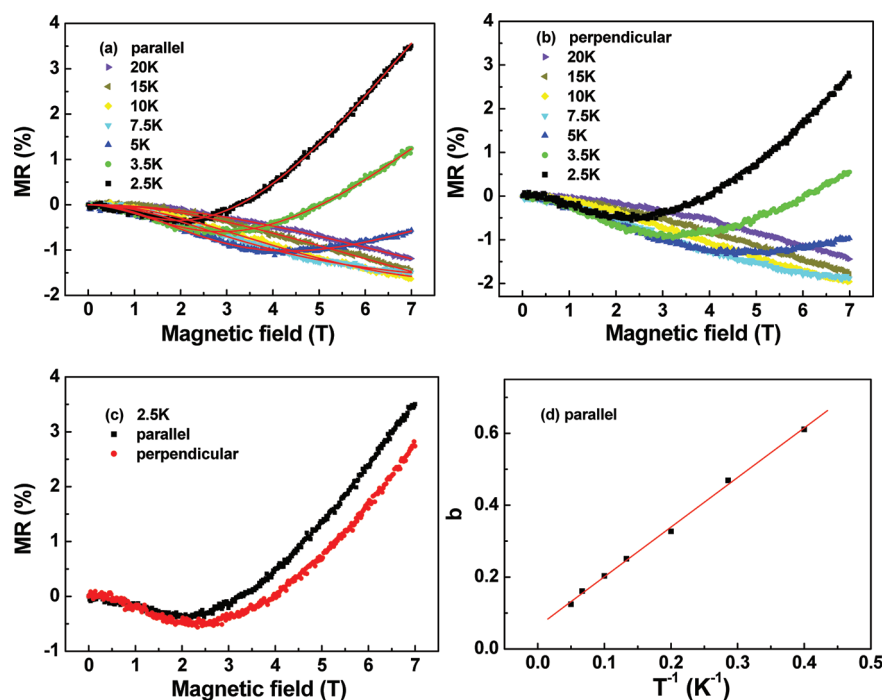


Figure 4. MR of an Al-implanted ZnO NW at different temperature. The magnetic field is oriented parallel (a) and perpendicular (b) to the axis of NW. The red curves in (a) are least-squares fitting using eq 3. (c) Comparison of the parallel and perpendicular MR at 2.5 K. (d) Fitting parameter b (see eq 3) as a function of inverse temperature. The red line corresponds to a linear fitting of the data.

At liquid helium temperature, the implanted ZnO NWs still reveal a very weak gate effect, similar to the one observed at room temperature. The current–voltage (I – V) characteristics presented in Figure 2a do not present any Schottky-type contact behavior even at 2.5 K, which again confirms the good ohmic quality of the contacts. The differential conductance shows, however, a strong dependence on temperature. In Figure 2b,c we plot the differential conductance $dI/dV(V)$ at different temperatures for Al- and Co-implanted NWs, respectively. A zero bias anomaly is clearly observed in the Co-implanted NW, and this anomaly becomes considerably weaker in the Al-implanted NW. The origin of the anomaly can be linked to a suppression of the density of states at the Fermi level due to disorder enhanced electron–electron (e–e) interaction at low temperatures.²⁵ This anomaly is usually detected by measuring the temperature dependence of the electrical resistance but can also be probed by increasing the applied voltage, which gives rise to an increase of the electron temperature.²⁶ As discussed in more detail below, we link the larger suppression of the density of states in the Co-implanted

NWs to the narrower conduction channel when compared to the Al-implanted NWs, which results in a more pronounced 1D electrical conduction with increased e–e interaction. This is not unexpected since the ion implantation range and ion straggle of the Co (37 and 16 nm) are smaller than for Al (68 and 32 nm) due to the different atomic number. Moreover, Al is a more effective and shallow donor than Co. Finally, Al ions diffuse easier during the postannealing process due to their smaller size, making the conduction channel considerably wider.

Further evidence for the presence of disorder enhanced e–e interaction is provided by our measurements of the temperature dependence of the electrical resistance. As already mentioned above, the resistance of the implanted NWs only increases by a factor of 1–2 when cooling down from room temperature to liquid helium temperature. This weak temperature dependence cannot be explained in terms of hopping or another thermally activated transport mechanism. We therefore interpret the low-temperature electrical transport in our implanted NWs in the framework of quantum corrections effects in disordered systems, i.e., weak localization and disorder

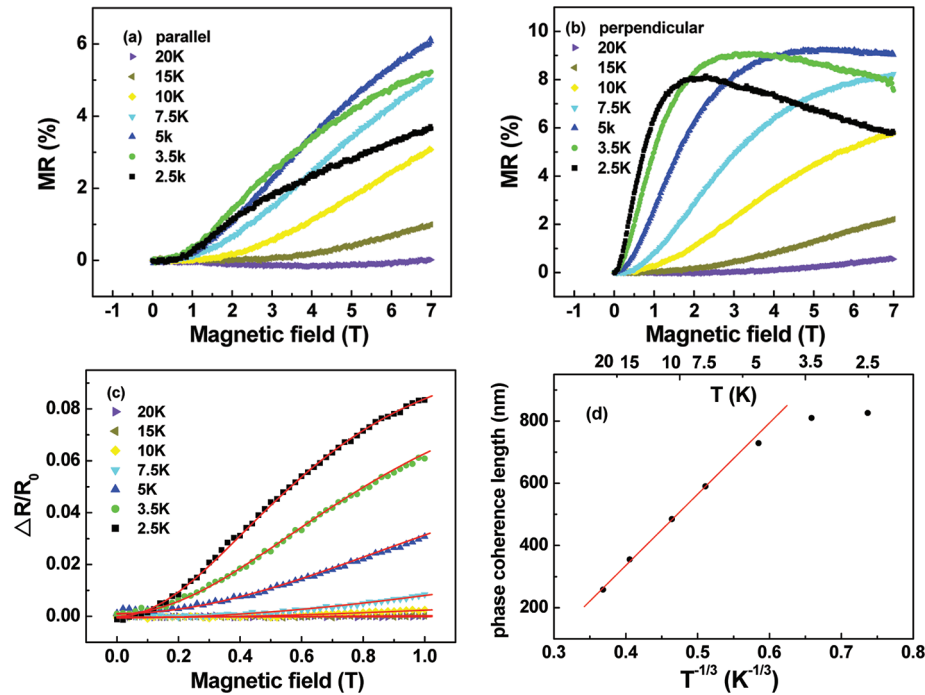


Figure 5. MR of a Co-implanted ZnO NW at different temperatures. The magnetic field is oriented parallel (a) and perpendicular (b) to the axis of NW. (c) Difference between the perpendicular and parallel MR at different temperatures. The red curves are the result of least-squares fitting using eq 4. (d) Phase coherence length as a function of temperature.

enhanced e–e interaction.²⁵ In 1D systems the contribution of the e–e interaction to the resistance is given by^{27,28}

$$\frac{\Delta R}{R_0} = \frac{\rho_e e^2}{2^{3/2} \pi \hbar A} \left(4 - \frac{3}{2} F \right) \left[\frac{D \hbar}{k_B T} \right]^{1/2} \quad (1)$$

while in 3D systems, the effect of the e–e interaction changes to^{25,28}

$$\Delta R = \frac{1.3 \rho_e e^2}{4 \pi^2 \sqrt{2} \hbar} \left(\frac{4}{3} - \frac{3}{2} F \right) \left[\frac{k_B T}{D \hbar} \right]^{1/2} \quad (2)$$

where F describes the strength of the screening of the e–e interaction. The length scale $L_T = (D \hbar / k_B T)^{1/2}$ is referred to as the thermal length, which determines the system dimensionality for e–e interaction based effects. In Figures 3a,b we plot the resistance of implanted NWs for temperatures below 20 K as a function of $T^{-1/2}$ and $T^{1/2}$, respectively. The resistance of the Co-implanted NWs scales with $T^{-1/2}$, as expected for 1D e–e interaction at low temperatures. The deviation of the resistance at the lowest temperatures may result from spin–orbit scattering, which will be discussed in more detail below when interpreting the MR measurements. On the other hand, the temperature dependence of the resistance of the Al-doped NWs scales with $T^{1/2}$ below 20 K, which is consistent with the presence of 3D e–e interaction-induced corrections of the resistance. The observed temperature-dependent behaviors are therefore in good agreement with the above-mentioned conjecture, i.e., Co-implanted NWs are in the 1D conduction regime, while Al-doped NWs are in the 3D conduction regime. It should be emphasized that the agreement with the e–e interaction-based effects does not rule out the possibility that weak localization contributes to the temperature dependence of the resistance as well. As a matter of fact, weak localization in 1D gives rise to effects very similar to that of e–e interaction-

based effects. Measuring the temperature dependence of the resistance is therefore not sufficient to distinguish between weak localization and e–e interaction. A detailed analysis of the MR measurements is essential to properly distinguish between the two contributions to the resistance.

In Figures 4a,b we plot the MR of an Al-implanted ZnO NW at different temperatures, where the magnetic field is oriented parallel and perpendicular to the axis of the NW, respectively. At low temperatures between 2.5 and 5 K, the MR is first negative and then becomes positive at higher magnetic field. At higher temperatures, the MR is negative all the way up to 7 T. The negative MR at low magnetic fields appears to be quite insensitive to temperature. The observed behavior is difficult to explain in terms of weak localization and/or e–e interaction-based effects, which indicates that quantum corrections effects result in a limited contribution to the MR in our Al-implanted NWs. In Figure 4c, we compare the MR at 2.5 K for both orientations of the magnetic field. The MR is almost isotropic, except that the perpendicular MR becomes more “negative” at a higher magnetic field. One possible explanation is that the gradual transition from 3D to 1D occurs at lower temperatures due to the increased phase coherence length. Weak localization is expected to be enhanced in the perpendicular direction provided we are dealing with a 1D system. However, further quantitative information is difficult to extract due to the large background MR which dominates at higher fields. Instead we fit the parallel MR with a semiempirical model developed for degenerate In-doped CdS:²⁹

$$\frac{\Delta \rho}{\rho_0} = -a^2 \ln(1 + b^2 B^2) + \frac{c^2 B^2}{1 + d^2 B^2} \quad (3)$$

The negative MR component results from spin scattering related to doping induced local magnetic moments and is obtained when taking into account the third-order term for the

s–d exchange Hamiltonian. The positive MR component is related to the magnetic field induced change in the relative population of two conduction bands with different conductivities and relaxation times. This semiempirical model has been applied before to describe the MR of Ga-³⁰ and Co-doped ZnO thin films.³¹ A least-squares fitting gives the red curves in Figure 4a, revealing a good agreement with the experimental data. According to the model, the fitting parameter b should decrease with increasing temperature following a T^{-1} power law.^{29,30} In Figure 4d we plot the fitting parameter b as a function of inverse temperature, which clearly confirms the linear dependence of b on T^{-1} . The MR results confirm that the Al-implanted NWs behave as 3D, i.e., “bulk”, conductors.^{30,31}

We now turn to the MR of a Co-implanted ZnO NW, which is presented in Figure 5a,b for parallel and perpendicular geometry, respectively. Because the Co-implanted NWs behave as a 1D conducting channel, we first look at the parallel geometry, where weak localization has only a minor influence.²⁵ Unlike for Al-implanted NWs, the parallel MR of Co-implanted NWs does not depend in a monotonic way on temperature, which indicates the presence of both a negative and positive MR. We link the negative MR to spin-disorder and spin-flip scattering due to the Co doping. On the other hand, the origin of the positive MR is more complicated. In addition to the two-band model, as in the case of Al-implanted NWs, spin splitting due to disorder enhanced e–e interaction also gives rise to a positive MR, which is expected to be considerably enhanced in a 1D system.²⁵ Furthermore, the exchange interaction between the s-electrons (conduction electrons) and the electrons localized on the d-shell of the implanted transition-metal ions induces a giant spin splitting of the conduction band. This so-called s–d exchange-induced spin splitting will result in a sizable positive MR, which has been observed before in transition-metal-doped ZnO thin films.^{16,20} We note that in spite of the clear presence of a negative MR due to the Co doping, the overall positive MR of the Co-implanted NWs is larger than that of the Al-implanted NWs. We therefore believe that the positive MR of the Co-implanted NWs is the combined effect of the different contributions discussed above.

The perpendicular MR is again not varying monotonically with temperature at higher magnetic fields, which is due to the interplay of the negative and positive MR, similar to the case of the parallel geometry. On the other hand, the perpendicular geometry gives rise to a larger MR and to additional interesting features at low temperature. There occurs a large onset of positive MR at low magnetic fields, and this MR changes into a negative MR at higher magnetic fields. We assign this anisotropic MR to weak localization, which occurs only for the perpendicular geometry in a 1D system. Weak electron localization originates from the constructive interference between backscattered electronic wave functions along time-reversed paths. This phenomenon manifests itself by a positive correction of the electrical resistance at zero magnetic field, which is easily destroyed by applying a magnetic field. On the other hand, spin–orbit scattering introduces changes of the spin states of the electrons, which preserve time-reversal symmetry but influence the sign of the interference term. Strong spin–orbit scattering changes the sign of the contribution of weak localization to the resistance and causes a pronounced positive MR, known as weak antilocalization.³² We therefore assume that the large onset of positive MR for the perpendicular geometry is due to the presence of strong spin–orbit scattering.

However, the above-mentioned interplay between negative and positive MR leads to difficulties in better understanding the observed MR. We therefore interpret our data in the following way. Assuming that the MR resulting from e–e interaction and magnetic scattering as well as the MR predicted by the semiempirical model (eq 3) are isotropic, we extract the MR which is due to weak electron localization by subtracting the parallel MR from the perpendicular MR. We plot the result of this subtraction in Figure 5(c), where we observe a monotonic variation with temperature. We fit this MR using the model for 1D weak electron localization in the presence of spin–orbit scattering:^{28,33,34}

$$\frac{\Delta R}{R_0} = \frac{\rho_e e^2}{2\pi\hbar A} \left[\frac{3}{2} \left(L_\phi^{-2} + \frac{4}{3} L_{SO}^{-2} + L_H^{-2} \right)^{-1/2} - \frac{1}{2} (L_\phi^{-2} + L_H^{-2})^{-1/2} \right] \quad (4)$$

where L_ϕ and L_{SO} are the phase coherence length and spin–orbit diffusion length, respectively. The magnetic length $L_H = (3\hbar^2/e^2AH^2)^{1/2}$, where A is the cross-sectional area of the NW. Both L_ϕ and L_H need to be larger than the transverse dimension of the nanowires (d) to be in the 1D regime. We use L_ϕ , L_{SO} , and d as three fitting parameters and only consider magnetic fields smaller than 1 T to make sure that $L_H > d$. The least-squares fitting curves are plotted as red curves in Figure 5c, revealing good agreement with the experimental data. The fittings for different temperatures result in a spin–orbit diffusion length of 300 ± 20 nm and a d value of 6 ± 1 nm, with negligible dependence on temperature. The small value of d is due to the rather limited depth for the Co implantation (ion straggle of 16 nm). Moreover, we assume that only the region with the highest Co implantation dominates the conductance of the Co-implanted NWs. This is confirmed by the fact that the Co-implanted NWs with a small fluence of 5×10^{15} ions/cm² have a very high resistance, i.e., hundreds of MΩ at low temperature.

As becomes clear from Figure 5d, the phase coherence length obtained from the fitting decreases with increasing temperature. There exist various dephasing mechanisms in disordered systems, depending on the system dimensionality, the level of disorder, and the temperature.³⁵ At low temperatures in metals and semiconductors, small energy transfer e–e scattering is the dominant dephasing process, giving rise to a scattering rate $1/\tau_{ee} \propto T$ in 2D systems, and $1/\tau_{ee} \propto T^{2/3}$ in 1D systems. This dephasing is commonly known as the Nyquist dephasing mechanism.³⁶ We then obtain a phase coherence length $L_\phi = (D\tau_\phi)^{1/2}$ which scales with $T^{-1/3}$ in 1D, in agreement with the observed temperature dependence between 5 and 20 K in Figure 5d. In our Co-implanted NWs not only inelastic scattering but also magnetic scattering will destroy the phase coherence. The total phase-breaking rate is given $\tau_\phi^{-1} = \tau_{in}^{-1} + 2\tau_s^{-1}$, where τ_{in}^{-1} and τ_s^{-1} are the inelastic scattering rate (corresponding to τ_{ee}^{-1} in our case) and the magnetic scattering rate, respectively.^{28,32} Consequently, the saturation of the phase coherence length in Figure 5d below 5 K can be attributed to the fact that the magnetic scattering rate becomes dominant at lower temperatures. We also note that at the highest magnetic fields both the parallel and perpendicular MR reach their maximum value at 5 K and become smaller at 2.5 K (Figures 5a,b), which provides additional evidence for the dominance of

the magnetic scattering below 5 K. The increased negative MR resulting from magnetic scattering cancels the overall positive MR at low temperature. We therefore conclude that the electrical transport in our Co-implanted ZnO NWs is considerably influenced by 1D weak localization in the presence of strong spin–orbit scattering as well as strong magnetic scattering.

Finally, we want to stress a few more points. It has been shown before that the spin–orbit scattering cross section depends on the atomic number Z according to a power law Z^5 . Moreover, the spin–orbit scattering cross section also depends on the valence of the impurity, e.g., the scattering is considerably smaller for s-type impurities than for p-type impurities.³⁷ As discussed in the framework of Figure 1b, the conductivity of the NWs results from the implanted dopants. The strong spin–orbit scattering in Co-implanted NWs can then be linked to the larger atomic number of Co (27) than of Al (13). On the other hand, the valence electrons of the Co may further enhance the spin–orbit scattering in the ZnO host. Taking into account the spin–orbit scattering, it is easy to understand the deviation of the resistance in the Co-implanted NWs at the lowest temperatures (Figure 3a). As demonstrated in Figure 3c, weak antilocalization induced by the spin–orbit scattering is enhanced at lower temperatures. Weak antilocalization will change the sign of the contribution of weak localization to the resistance. Therefore, the resistance tends to saturate as a result of the opposing contributions of the weak antilocalization and the disorder enhanced e–e interaction.

From our experimental results we extract a large phase coherence length up to 800 nm at 2.5 K (see Figure 5d), which is larger than for In-doped ZnO NWs (56.3 nm at 4.2 K)³⁸ and even larger than for nominally undoped ZnO nanoplates (50–100 nm at 1.9 K)³⁹ and “natively” doped (doping induced by disorder) ZnO NWs (30 nm at 4.2 K).⁴⁰ ZnO is a wide bandgap semiconductor, implying the conductivity in nominally undoped ZnO can only be explained by the presence of a large amount of intrinsic and/or extrinsic defects. These defects, regardless of their origin, imply that the semiconductor is in the “dirty” limit with a considerable decrease of the phase coherence length. On the other hand, our virgin ZnO NWs do not show conductivity under dark conditions, which suggests a significant reduction of the number of defects. Therefore, our Co-implanted ZnO NWs retain a larger phase coherence length than the nominally undoped ones.^{39,40} Recently, Hsu et al. also reported a large phase coherence length in single indium tin oxide NWs (520 nm at 0.25 K),⁴¹ which confirms that a very large phase coherence length can be obtained in oxide NWs. Interestingly, Hsu et al. observed 1D weak localization as well as weak antilocalization depending on the resistivity of the samples. We may expect similar phenomena in our implanted ZnO wires if we are able to control the resistivity of the ZnO NWs within a wider range.

In conclusion, we presented a straightforward method to tune the electrical as well as the magnetotransport properties of ZnO NWs by ion implantation. The virgin NWs are configured as FETs that are in the enhancement mode. The Al- and Co-implanted NWs reveal metallic-like behavior with quantum corrections appearing at low temperature. We demonstrate that the electrical transport of individual NWs can be changed from 3D (Al-implanted) to 1D (Co-implanted). In particular, the anisotropic magnetoresistance of Co-implanted NWs results from 1D weak localization in the presence of strong spin–orbit coupling. We obtain a large phase coherence length up to 800

nm at low temperature, which is of direct interest for spintronics-related applications. The presented doping method, which relies on ion implantation, is in principle also applicable to other nanomaterials for electrical as well as for magnetic modulation.

AUTHOR INFORMATION

Corresponding Author

*E-mail: yujia.zeng@fys.kuleuven.be.

ACKNOWLEDGMENTS

This work has been supported by the Research Foundation–Flanders (FWO, Belgium), by the Belgian Interuniversity Attraction Poles research program (IAP P6/42), and by the K.U. Leuven through the Concerted Research Action program (GOA/09/006) and the Centers of Excellence program (INPAC, grant no. EF/05/005).

REFERENCES

- (1) Lu, W.; Lieber, C. M. *Nat. Mater.* **2007**, *6*, 841.
- (2) Hochbaum, A. L.; Yang, P. D. *Chem. Rev.* **2010**, *110*, 527.
- (3) Wang, Z. L. *Mater. Sci. Eng. R-Rep.* **2009**, *64*, 33.
- (4) Barth, S.; Hernandez-Ramirez, F.; Holmes, J. D.; Romano-Rodriguez, A. *Prog. Mater. Sci.* **2010**, *55*, 563.
- (5) Lu, J. G.; Chang, P. C.; Fan, Z. Y. *Mater. Sci. Eng., R-Rep.* **2006**, *52*, 49.
- (6) Özgür, Ü.; Alivov, Y. I.; Liu, C.; Teke, A.; Reshchikov, M. A.; Doğan, S.; Avrutin, V.; Cho, S. J.; Morkocd, H. *J. Appl. Phys.* **2005**, *98*, 041301.
- (7) Janotti, A.; Van de Walle, C. G. *Rep. Prog. Phys.* **2009**, *72*, 126501.
- (8) Klingshirn, C.; Fallert, J.; Zhou, H.; Sartor, J.; Thiele, C.; Maier-Flaig, F.; Schneider, D.; Kalt, H. *Phys. Status Solidi B* **2010**, *247*, 1424.
- (9) Wang, Z. L.; Song, J. H. *Science* **2006**, *312*, 242.
- (10) Heo, Y. W.; Norton, D. P.; Tien, L. C.; Kwon, Y.; Kang, B. S.; Ren, F.; Pearton, S. J.; LaRoche, J. R. *Mater. Sci. Eng., R-Rep.* **2004**, *47*, 1.
- (11) Bao, J. M.; Zimmler, M. A.; Capasso, F.; Wang, X. W.; Ren, Z. F. *Nano Lett.* **2006**, *6*, 1719.
- (12) Levy-Clement, C.; Tena-Zaera, R.; Ryan, M. A.; Katty, A.; Hodes, G. *Adv. Mater.* **2005**, *17*, 1512.
- (13) Dietl, T.; Ohno, H.; Matsukura, F.; Cibert, J.; Ferrand, D. *Science* **2000**, *287*, 1019.
- (14) Awschalon, D. D.; Flatte, M. E. *Nat. Phys.* **2007**, *2*, 153.
- (15) Zutic, I.; Fabian, J.; Das Sarma, S. *Rev. Mod. Phys.* **2004**, *76*, 323.
- (16) Andrearczyk, T.; Jaroszyński, J.; Grabecki, G.; Dietl, T.; Fukumura, T.; Kawasaki, M. *Phys. Rev. B* **2005**, *72*, 121309(R).
- (17) Tian, Y. F.; Yan, S. S.; Cao, Q.; Deng, J. X.; Chen, Y. X.; Liu, G. L.; Mei, L. M.; Qiang, Y. *Phys. Rev. B* **2009**, *79*, 115209.
- (18) Sharma, N.; Granville, S.; Kashyap, S. C.; Ansermet, J.-Ph. *Phys. Rev. B* **2010**, *82*, 125211.
- (19) Ye, S.; Ney, V.; Kammermeier, T.; Ollefs, K.; Zhou, S.; Schmidt, H.; Wilhelm, F.; Rogalev, A.; Ney, A. *Phys. Rev. B* **2009**, *80*, 245321.
- (20) Xu, Q. Y.; Hartmann, L.; Schmidt, H.; Hochmuth, H.; Lorenz, M.; Spemann, D.; Grundmann, M. *Phys. Rev. B* **2007**, *76*, 134417.
- (21) Liang, W. J.; Yuhas, B. D.; Yang, P. D. *Nano Lett.* **2009**, *9*, 892.
- (22) Perea, D. E.; Hemesath, E. R.; Schwalbach, E. J.; Lensch-Falk, J. L.; Voorhees, P. W.; Lauhon, L. J. *Nat. Nanotechnol.* **2009**, *4*, 315.
- (23) Zeng, Y. J.; Menghini, M.; Li, D. Y.; Lin, S. S.; Ye, Z. Z.; Hadermann, J.; Moorkens, T.; Seo, J. W.; Locquet, J.-P.; Van Haesendonck, C. *Phys. Chem. Chem. Phys.* **2011**, *13*, 6931.
- (24) Ziegler, J. F.; Biersack, J. P.; Littmark, U. *The stopping and range of ions in solids*; Pergamon Press: New York, 1985.
- (25) Lee, P. A.; Ramakrishnan, T. V. *Rev. Mod. Phys.* **1985**, *57*, 287.
- (26) Bishop, D. J.; Tsui, D. C.; Dynes, R. C. *Phys. Rev. Lett.* **1980**, *44*, 1153.
- (27) Altshuler, B. L.; Aronov, A. G.; Lee, P. A. *Phys. Rev. Lett.* **1980**, *44*, 1288.

- (28) Beutler, D. E.; Giordano, N. *Phys. Rev. B* **1988**, 38, 8.
- (29) Khosla, R. P.; Fischer, J. R. *Phys. Rev. B* **1970**, 2, 4084.
- (30) Reuss, F.; Frank, S.; Kirchner, C.; Kling, R.; Gruber, Th.; Waag, A. *Appl. Phys. Lett.* **2005**, 87, 112104.
- (31) Gacic, M.; Jakob, G.; Herbort, C.; Adrian, H.; Tietze, T.; Brück, S.; Goering, E. *Phys. Rev. B* **2007**, 75, 205206.
- (32) Bergmann, G. *Phys. Rep.* **1984**, 107, 1.
- (33) Al'tshuler, B. L.; Aronov, A. G. *Pis'ma Zh. Eksp. Teor. Fiz.* **1981**, 33, 515; *JETP Lett.* **1981**, 33, 499.
- (34) Santhanam, S.; Wind, S.; Prober, D. E. *Phys. Rev. Lett.* **1984**, 53, 1179.
- (35) Lin, J. J.; Bird, J. P. *J. Phys.: Condens. Matter* **2002**, 14, R501.
- (36) Al'tshuler, B. L.; Aronov, A. G.; Khmelnitsky, D. E. *J. Phys. C: Solid State Phys.* **1982**, 15, 7367.
- (37) Geier, S.; Bergmann, G. *Phys. Rev. Lett.* **1992**, 68, 2520.
- (38) Thompson, R. S.; Li, D. D.; Witte, C. M.; Lu, J. G. *Nano Lett.* **2009**, 9, 3991.
- (39) Likovich, E. M.; Russell, K. J.; Eric W. Petersen, E. W.; Narayanamurti, V. *Phys. Rev. B* **2009**, 80, 245318.
- (40) Chiu, S. P.; Lin, Y. H.; Lin, J. J. *Nanotechnology* **2009**, 20, 015203.
- (41) Hsu, Y. W.; Chiu, S. P.; Lien, A. S.; Lin, J. J. *Phys. Rev. B* **2010**, 82, 195429.